PHOTONICS Research

Complete crossing of Fano resonances in an optical microcavity via nonlinear tuning

Martino Bernard,[1,2,*] Fernando Ramiro Manzano,[2] Lorenzo Pavesi,[2] Georg Pucker,[1]
Iacopo Carusotto,[3] and Mher Ghulinyan[1]

[1]*Centre for Materials and Microsystems, Fondazione Bruno Kessler, I-38123 Povo, Italy*
[2]*Department of Physics, Nanoscience Laboratory, University of Trento, I-38123 Povo, Italy*
[3]*INO-CNR BEC Center and Department of Physics, University of Trento, I-38123 Povo, Italy*
*Corresponding author: martino.bernard@unitn.it

We report on the modeling, simulation, and experimental demonstration of complete mode crossings of Fano resonances within chip-integrated microresonators. The continuous reshaping of resonant line shapes is achieved via nonlinear thermo-optical tuning when the cavity-coupled optical pump is partially absorbed by the material. The locally generated heat then produces a thermal field, which influences the spatially overlapping optical modes, allowing us to alter the relative spectral separation of resonances. Furthermore, we exploit such tunability to continuously probe the coupling between different families of quasi-degenerate modes that exhibit asymmetric Fano interactions. As a particular case, we demonstrate a complete disappearance of one of the modal features in the transmission spectrum as predicted by Fano [Phys. Rev. 124, 1866 (1961)]. The phenomenon is modeled as a third-order nonlinearity with a spatial distribution that depends on the stored optical field and thermal diffusion within the resonator. The performed nonlinear numerical simulations are in excellent agreement with the experimental results, which confirm the validity of the developed theory.   © 2017 Chinese Laser Press

1. INTRODUCTION

On-chip microcavities have been proven of significant interest to the development of photonics for telecommunications [1,2]. Their ability to confine electromagnetic radiation and enhancement of light–matter interactions makes them suitable for signal filtering and nonlinear frequency generation processes, while the compatibility with the silicon platform opens the possibility for scalability [3–5]. Delay lines, memories, modulators, and frequency comb sources have been demonstrated in microresonator devices within the silicon platform [6–9]. For practical applications, in order to select desired wavelengths, spectral tunability of the resonant features is required. This is often achieved via electrical micro-heaters that exploit the thermo-optic effect to modify the refractive index of the environment, thus changing the optical path of the device [10]. The thermo-optical tuning can be applied to a variety of materials systems, from silicon to silicon nitrides and oxynitrides and is applicable to a wide range of operation wavelengths. This kind of approach, however, has a global action and does not allow us to tune spectral channels separately. Altering the transmission of a selected single resonance has been demonstrated, for example, by exploiting

inverse Raman scattering in Si devices [11,12]. As opposed to thermo-optical tuning, this effect is strongly selective to the operation frequencies because the Raman frequency and bandwidth depend primarily on the material choice.

Here we propose an all-optical approach to relatively detune the resonances within a microresonator by exploiting the thermo-optical effect at a local level. The effect is demonstrated by applying it to a whispering gallery resonator-waveguide system, which exhibits Fano interference features [6,13–18]. The continuous detuning is used to explore complete mode crossings between two resonances. As a particular example, this fine tuning approach allows us to access the complete destructive interference point on one side of the Fano line shape, where one of the resonances disappears from the spectrum, as predicted in Ref. [18].

The paper is structured as follows: Section 2 starts with a brief theoretical summary of the system under study. The generic thermo-optic effect is described in Section 2.A and then, in Section 2.B, introduced into the dynamic equations for the field amplitude in the resonator to demonstrate the tuning of a single resonance. The model is then extended to

interacting modes in Section 2.C. In Section 3 we report the experimental results, while Section 4 exposes the numerical simulations that match the model with the experiment. Finally, Section 5 gives the summary of our results and the conclusions.

2. THEORY

The wave equation inside a circular-shaped microresonator may be separated into three 1D equations with quantum numbers z, R, and M for the axial, radial, and azimuthal coordinates, respectively. The resonator is considered to be single-mode in the axial direction ($z = 1$). The set of modes with different azimuthal number M but with the same radial number $R = n$ is addressed as nth-radial mode family, denoted with R_n. Here, we will consider only $R = 1$ and $R = 2$ for the radial direction. For each radial family, the frequency of the Mth mode may be calculated as
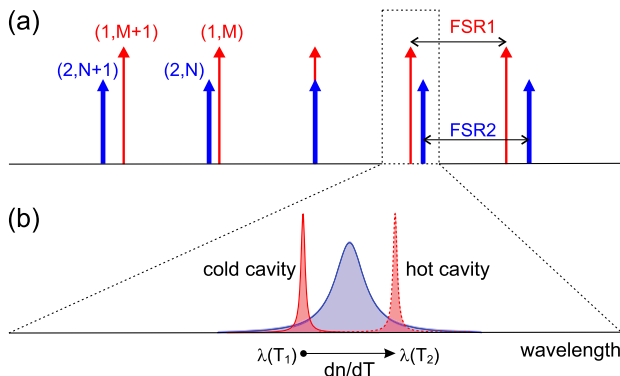
$$\omega_M = \frac{2\pi c M}{n_{\text{eff}}(z, R, M)L},\qquad(1)$$

where L is the geometrical path of the light in the resonator, typically the circumference, $n_{\text{eff}}(z, R, M)$ is the effective refractive index of the mode, and c is the light velocity in vacuum.

The resonator is excited and probed by a waveguide. The transmission spectrum of the waveguide-resonator system exhibits a series of negative peaks, due to the capture of the modes by the resonator, where the azimuthal modes are spaced by the free spectral range (FSR):

$$\text{FSR}(\omega_M) = \frac{2\pi c}{n_g^M L},\qquad(2)$$

with n_g^M being the group velocity of the Mth mode. Equation (1) implies that, within a single radial family, modes with different M lay at different frequencies, preventing photon exchange between such modes. When different radial families are present, however, there may be combinations of R and M, which give spectrally overlapping modes [Fig. 1(a)]. While the spectral overlap may be an undesired feature [12], it also may

provide new interesting physics if an interaction among the degenerate modes is provided [18].

Here, we will take into account the interference phenomena due to waveguide-mediated interactions among the modes of different radial families, leading to asymmetric Fano resonances and energy shifts of the modes. In order to observe the Fano interference, spectral overlap between a pair of modes belonging to different radial families is required. This means that $\Delta\omega = \omega_2 - \omega_1$, relative distance between the central frequency of two modes ω_2 and ω_1, respectively, should be at most of the same order of the largest half-width at half maximum (HWHM) between the two modes:

$$|\Delta\omega| \lesssim \max(\text{HWHM}_1, \text{HWHM}_2).\qquad(3)$$

Figure 1(a) shows schematically that each radial mode family is a comb of peaks obeying Eq. (1), which are spaced spectrally by FSR according to Eq. (2):

$$\omega_{M+l}^1 \simeq \omega_M^1 + l \cdot \text{FSR}_1,\qquad(4a)$$

$$\omega_{N+l}^2 \simeq \omega_N^2 + l \cdot \text{FSR}_2,\qquad(4b)$$

where $l = \pm 1, \pm 2, \dots$. Because, in general, n_g is different for different radial families, the FSRs also will differ. This means that the two radial mode combs will slide spectrally one against the other, similar to a Vernier scale [19], passing though a crossing point. The relative detuning $\delta\omega^{12}$ of two modes in the couple is thus

$$\delta\omega_l^{12} = \omega_{M+l}^1 - \omega_{N+l}^2 \simeq \delta\omega_0^{12} + l \cdot \Delta\text{FSR}_{12},\qquad(5)$$

where $\delta\omega_0^{12} = \omega_M^1 - \omega_N^2$ is the relative detuning of the (MN) couple and $\Delta\text{FSR}_{12} = \text{FSR}_1 - \text{FSR}_2$.

Having couples of modes of two radial families with different relative detuning permits us to monitor the coupling between the two radial families when changing the M with a discrete step of ΔFSR_{12} just by changing M. This has been studied in detail in our previous work [18].

The Fano interaction of two resonances offers rich physics and is extremely sensitive to both the degree and the sign of the detuning $\delta\omega_l^{12}$. The asymmetric Fano line shape may vary abruptly with changing the detuning due to the fine interplay of the phases of individual resonances. For example, there exists a unique spectral point on one side of the composite resonance, where a particular destructive interference leads to full suppression of one of the transmission features in the spectrum [18,20]. This situation may be observed experimentally in fortuitous cases for which a given ΔFSR_{12} exactly satisfies the necessary condition. On the other hand, the particular point always can be observed if the detuning can be continuously varied within a single couple of resonances.

In the following, we demonstrate a continuous method to detune the relative frequency of a couple of modes, allowing complete mapping of the interaction within a single couple of resonances, as sketched in Fig. 1(b). Moreover, this approach permits us to finely tune and capture the particular point of resonance suppression.

A. Thermo-Optic Effect

Here we propose to use the thermo-optic effect [12,21,22] as a tool to tune the relative frequency of the resonator's modes. For small variations around room temperature, the thermo-optic

Fig. 1. Schematic representation of the mode-crossing possibilities. (a) Azimuthal modes of two radial families progressively shift at each increment of the azimuthal number due to the difference in FSR, possibly going through a crossing. (b) Continuous tuning of a doublet of resonances may be obtained via nonlinearities, such as a localized thermo-optic effect.

coefficient dn/dT may be defined as the first Taylor expansion of the refractive index of the material as a function of the temperature. Heating the sample thus induces a variation in the effective refractive indices and coupling coefficients of the cavity modes, which are consequently shifted. Adding the thermo-optic coefficient dn/dT into Eq. (1), we obtain

$$\omega_M \approx \frac{2\pi c M}{L n_{\text{eff}}}\left(1 - \frac{dn_{\text{eff}}}{dT}\frac{\Delta T}{n_{\text{eff}}}\right) = \omega_M^0 + \delta\omega. \qquad (6)$$

With this definition, the usual positive thermo-optic coefficient makes the resonances shift toward the red (longer wavelengths) when heating the sample. When a high-power laser (hereafter, pump, p) is used to excite a doublet of resonances, a part of the energy is absorbed by the material by heating locally the resonator exactly in the spatial region where the modes extend. Heat then diffuses gradually over the whole device. Figure 2 shows a finite elements method (FEM) simulation of the temperature distribution inside the resonator when the electrical field distribution function $\mathcal{E}^p(r)$ of the first and second radial family modes is used as the thermal source. The respective spatial distribution functions of the electrical field of the modes $\mathcal{E}(r)$ are shown as contour lines in Figs. 2(a) and 2(b).

The thermal diffusion may be represented with a kernel functional $\chi(r, r')$ that takes into account for the absorption and thermal properties of the host materials. The temperature shift is also proportional to the square of the mode amplitude α^p. The thermal shift $\delta n(r)$ in the refractive index is therefore proportional to

$$\delta n(r) \propto \int \chi(r, r')|\alpha^p \mathcal{E}^p(r')|^2 dr'$$
$$\propto |\alpha^p|^2 \int \chi(r, r')|\mathcal{E}^p(r')|^2 dr'. \qquad (7)$$

Alongside, the effect of $\delta n(r)$ on the spectral shift of the weakly excited probe mode (hereafter, called s) depends on the spatial overlap of the probe mode's electrical field distribution $\mathcal{E}^s(r)$ with the pump-generated $\delta n(r)$:

$$\delta\omega \propto \int |\mathcal{E}^s(r)|^2 \delta n(r) dr. \qquad (8)$$

This frequency shift may be rewritten in terms of a constant g that incorporates the light–matter interaction and the spatial overlaps of the pump and probe modes mediated by the thermal kernel $\chi(r, r')$:
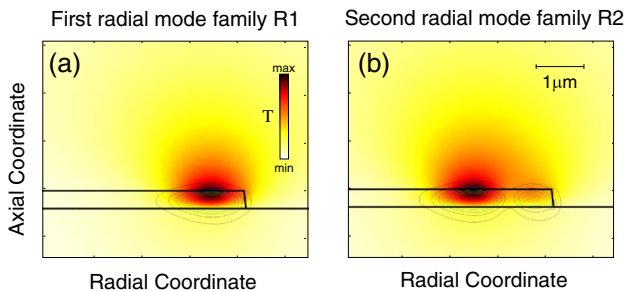
$$\delta\omega = |\alpha^p|^2 \int |\mathcal{E}^s(r)|^2 \int \chi(r, r')|\mathcal{E}^p(r')|^2 dr' dr = |\alpha^p|^2 g. \qquad (9)$$

A consequence of the proportionality of the spectral shift $\delta\omega$ to the mode intensity $|\alpha^p|^2$ is that the effect is stronger for modes with a higher quality factor, which exhibit stronger field enhancement.

B. Single Family Tuning

As discussed in the beginning, for each radial family, the spectral position of unperturbed azimuthal modes is given by Eq. (1). The spectral shape and the waveguide-induced perturbation effect of a generic mode i may be deduced by plugging the unperturbed resonance frequency ω_i^0 into the dynamic equation of the mode's intensity [18]:

$$\mathcal{L}_i(t) \equiv i\frac{d\alpha_i}{dt} = \left[\omega_i^o + \Delta_{ii} - i\frac{\gamma_i^{\text{nr}} + \Gamma_{ii}^{\text{rad}}}{2}\right]\alpha_i + \bar{f}_i E_{\text{inc}}(t), \qquad (10)$$

where α_i is the mode amplitude, Δ_{ii} is a self-interacting reactive term due to the presence of the coupling waveguide, γ_i^{nr} and Γ_{ii}^{rad} are the dissipative terms representing, respectively, the non-radiative and radiative losses of the mode, and $\bar{f}_i$ is the coupling strength between the waveguide and resonator. Here, $E_{\text{inc}}(t)$ is the incident field propagating in the waveguide, which we will take in the form $E_{\text{inc}}(t) = E_{\text{inc}} e^{-i\omega_{\text{inc}}t}$. The typical spectral shape of a resonance, calculated from Eq. (10) in a steady state and under weak excitation conditions, is a Lorentzian function (see the cold cavity case in Fig. 3).

Let us now introduce the intensity-dependent nonlinearity g of Eq. (9) in the resonator. The new dynamic equation for mode i reads

$$i\frac{d\alpha_i}{dt} = \mathcal{L}_i(t) + |\alpha_i|^2 g\alpha_i. \qquad (11)$$

Consider now dynamic pumping of the system, obtained, for example, by a strong tunable laser slowly scanning across the resonance from short to long wavelengths. When the pump reaches the resonance tail, the laser power enters the resonator,
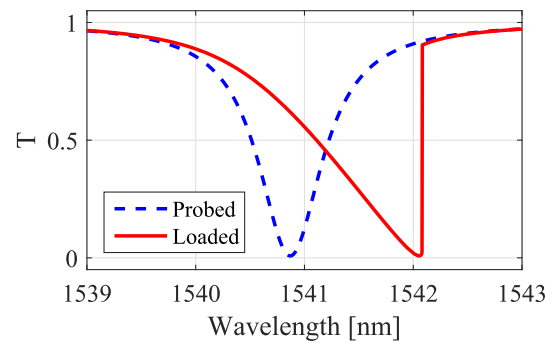
Fig. 3. Resonant line shape modification under a sweeping pump in the presence of optical nonlinearity. The cold cavity spectrum (dashed line) is obtained with a weak probe. When sweeping the spectrum using a high-power laser (solid line), the resonance shifts progressively due to the increasing nonlinear effect, resulting in a spectrum with an apparent discontinuity, where the cavity mode de-locks from the pump laser.

First radial mode family R1   Second radial mode family R2

Fig. 2. Simulated thermal distribution generated by (a) the first and (b) the second optical radial family modes. The contour lines show the modes' electric field profiles.

enabling the last term in Eq. (11). While the pump laser enters farther inside the resonance peak, the nonlinear term increases, and the resonance escapes from the laser line. The time evolution of the intensity results therefore in the peculiar triangular shape (Fig. 3, full line). When the peak is surpassed, the nonlinear term decreases, resulting in a sudden de-locking of the peak from the driving laser [22]. In addition to the self-interacting term g introduced above, other terms g_{ji} coupling the amplitude of ith mode to the intensity in the jth mode could be present, for example, when the system is pumped with a broadband source, which strongly excites more than one resonance at the same time. In this case, the system evolution is described by a series of nonlinear differential equations, coupled to each other by the nonlinear terms g_{ji}:

$$i\frac{d\alpha_i}{dt} = \mathcal{L}_i(t) + \sum_j |\alpha_j|^2 g_{ji}\alpha_i. \qquad (12)$$

The nonlinear interaction may be exploited to alter the spectral position of a resonance by acting on a different resonance of the same radial mode family. This can be achieved through a pump and probe experiment, where (a) a strong laser line excites a single control resonance, while (b) the linear spectral response of one or more resonances is monitored through a weak probe source. This last should be weak enough to guarantee that the terms, which are nonlinear in the probe amplitude ($\sim|\alpha_i|^2$), are negligible. In particular, it is possible to access the dynamics of a strongly pumped mode M by following the spectral shift of an $(M+l)$th linear resonance. Indeed, for the non-pumped modes, the dynamic equation becomes parametric with respect to the field amplitude in mode M:

$$i\frac{d\alpha_j}{dt} = \mathcal{L}_j(t) + |\alpha_M|^2 g_{Mj}\alpha_j. \qquad (13)$$

Because the spatial overlap integral of Eq. (9) is almost constant within the same radial family R_1, in Eq. (13) we may furthermore approximate all coefficients g_{Mj} to be the same g_{11} within a broad range of M's.

C. Tuning of Resonant Doublets

Consider now two different radial mode families, R_1 and R_2. Equation (12) is still valid, with the i, j indices now running over all of the modes of both families. This time, however, because of the different field distributions among the two radial families, more genuinely different coefficients will be present: the second radial family self-interaction term g_{22} and a cross-family interaction term $g_{12}(=g_{21})$. The fact that the coupling constants are different for the two radial families gives rise to a net detuning when a single resonance is pumped.

In the following, we will consider doublets of resonances of two families in a region of spectral overlap; hence, the pump power will be split among two modes according to Eq. (1) of Ref. [18]:

$$\mathcal{F}_j^p(t) = i\frac{d\alpha_j^p}{dt} = \mathcal{L}_j^p(t) + \left(\Delta_{12} - i\frac{\Gamma_{12}^{rad}}{2}\right)\alpha_{3-j}^p, \qquad (14)$$

where the index $j = 1, 2$ denotes all of the interacting modes of the doublet. Joining Eq. (14) with Eq. (12), the doublets may be described with two coupled nonlinear equations of motion for the pumped peaks, while the probe, acting on another

doublet, may be described with a linear equation, parametric with respect to the pump fields. For the two pump (p) resonances it holds

$$i\frac{d\alpha_j^p}{dt} = \mathcal{F}_j^p(t) + (g_{jj}|\alpha_j^p|^2 + g_{12}|\alpha_{3-j}^p|^2)\alpha_j^p, \qquad (15)$$

while for each couple of probe peaks (s), the probe equation reads

$$i\frac{d\alpha_j^s}{dt} = \mathcal{F}_j^s(t) + (g_{jj}|\alpha_j^p|^2 + g_{12}|\alpha_{3-j}^p|^2)\alpha_j^s. \qquad (16)$$

The set of equations Eqs. (15) and (16) provide a general description of the system during the pump and probe experiment.

3. EXPERIMENTAL RESULTS

### A. Sample Description and Experimental Setup

The theory described in the previous sections is supported by experimental results. The samples studied in this work were realized using standard silicon microfabrication tools, as detailed in our previous works [18,23,24]. The resonator is realized in silicon nitride material and is coupled vertically to the underlying waveguide. The vertical coupling configuration plays a critical role, which is explained in the following.

In a planar geometry, when all guiding components lay in the same plane, the waveguide always has a stronger coupling to the first radial family with respect to the second one. On the contrary, the vertical coupling technique permits us to control the relative vertical alignment of the components. In particular, by placing the waveguide deeper under the resonator it is possible to invert the coupling trend between the R_1 and R_2 families such that the R_2 modes are coupled to the waveguide stronger than R_1 modes [18,24]. The devices studied here were fabricated such that the waveguide is situated 400 nm under the resonator (vertical gap), 500 nm inward from the outer rim of the resonator (negative horizontal gap).

The experimental setup, sketched in Fig. 4, consists of a tunable laser (pump) and a broadband probe source (spontaneous emission from a booster amplifier, BOA). The laser is amplified through an erbium-doped fiber amplifier (EDFA) and used as the high-power heating source. It is then mixed with the broadband signal in a 3 dB coupler and injected into the waveguide through a lensed optical fiber. The transmitted signal at the output of the waveguide is then collected with another lensed fiber and 50:50 split between an optical spectrum analyzer (OSA) to acquire the probe spectrum and a germanium detector, which measures the overall transmitted intensity. The detector measures the combined transmitted power of both the BOA and the pump, but the contribution of the second is several orders of magnitude larger than the first, permitting us to measure the dynamic transmission spectrum of the pump. In addition, two variable optical attenuators (VOAs) are used to avoid damage to the detector and coupler fibers. The OSA, on the other hand, allows the measurement of the probe transmission spectra due to the BOA broadband signal (Fig. 5). In the following subsections we will describe the results of pump and probe experiments for two particular cases, namely, the full suppression of one of the doublet modes
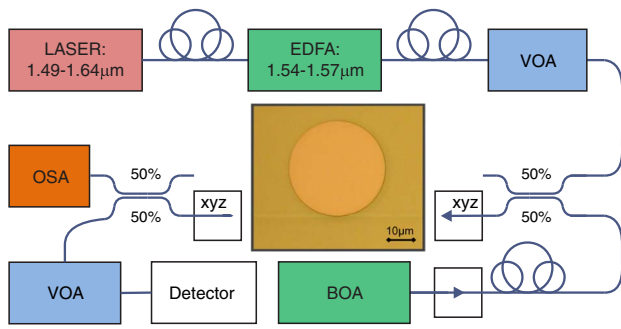
Fig. 4. Experimental setup. A tunable laser amplified with an EDFA is mixed with the broadband signal of a BOA and shone into the sample with a taper fiber. The output also is collected with a taper fiber, split, and fed to an OSA and a broadband germanium detector.
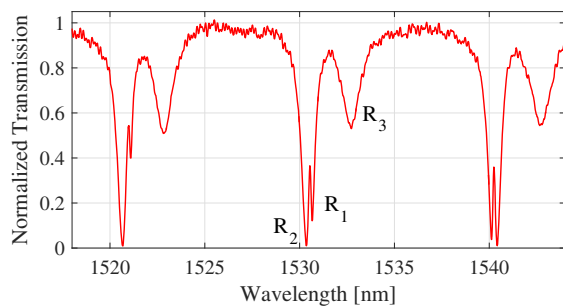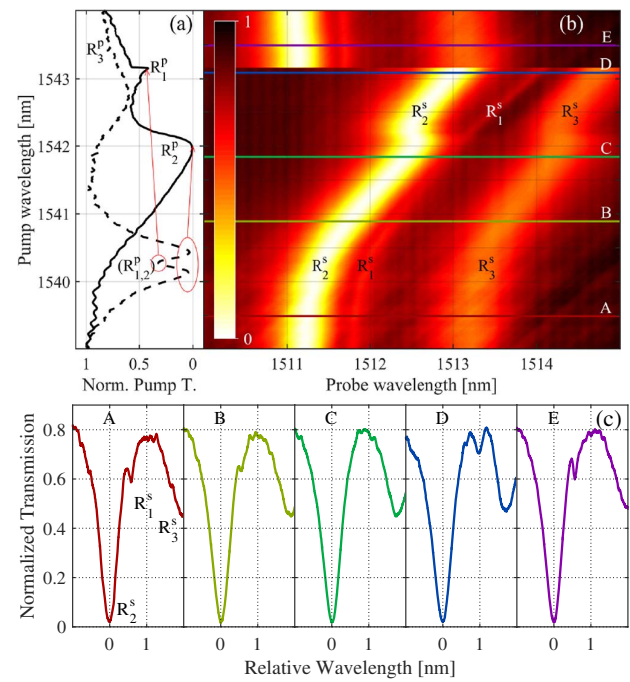

Fig. 5. Experimental cold cavity spectrum of the resonator. Three azimuthal modes are present for the families R_1, R_2, and R_3. The relative position of the R_1–R_2 doublet peaks transforms across the spectrum due to the difference in the respective FSRs.

Fig. 6. Results of the pump and probe experiment. Panel (a) shows the cold (dashed) and hot (solid) cavity transmission spectra of the device around the strongly pumped resonance doublet. The thermo-optic nonlinearity, induced by the pumped doublet, also affects the other resonances (b), allowing for a relative detuning of the peaks as shown by the transmission color map. (c) Selected transmission spectra show the transformation of the Fano resonance in the vicinity of the critical phase point, where a complete disappearance of the R_1^s peak feature takes place (panel C). The probe spectrum time-evolution, together with the pump dynamic transmission is represented in Visualization 1.

and the complete mode crossing in Fano resonances. In these experiments the sample was pumped with the EDFA in the region around a resonance doublet, while the broadband signal was used to probe the transmission of a different doublet. The dynamic evolution of the system was mapped by varying the pump laser wavelength by 10 pm steps and acquiring the probe spectrum over a time of 1 s. The resulting average pump sweeping speed, below 10 pm/s, ensures steady-state operation as the thermal decay time of the cavity is expected to be in the order of few microseconds [22].

B. Resonant Peak Suppression

Here we describe in detail the experiment where the rightmost doublet of Fig. 5 is pumped, while a doublet with a shorter wavelength is used as a probe. The chosen probe doublet forms a Fano resonance for which the relative detuning $\delta\omega_0^{12}$ of two modes is close to the critical interaction point, at which the narrow resonance is expected to be completely suppressed in the spectrum.

Figure 6(a) shows the dynamical transmission spectra of the resonances around 1540 nm, as the 2 W pump laser is shone through, scanning from short to long wavelengths. The cold cavity spectrum (dashed line) is the same as in Fig. 5, while it is worth noting that, in the pumped regime (solid line), both

the peaks R_2^p and R_1^p get dragged by the thermal detuning, giving the typical triangular shape.

An interesting feature, indicating that interaction is present, is the smooth de-locking of the R_2^p mode in favor of the R_1^p, right after the 1542 nm mark. The de-locking of the R_1^p mode, on the other side, is instantaneous, making a sharp jump partly eclipsed by the non-interacting third family. The effect is even more clearly visible in Fig. 6(b), where the probe resonance spectra as a function of the pump laser wavelength is mapped. As the pump is swept from short to long wavelengths, the probe resonances are continuously detuned accordingly. Because of the difference in the overlap with the thermal fields generated from the R_1^p and R_2^p modes, the two probe peaks gain a relative spectral shift. This shift is gradually changing the original value of $\delta\omega_0^{12}$, bringing the system to the critical point at which a complete disappearance of the R_1^s in the transmission spectra should take place. In fact, as a result of the fine tuning, we were able to experimentally validate the theoretical predictions from Ref. [18].

The relative shifts and the mode suppression are highlighted in Fig. 6(c), where selected spectral cross sections A–E of Fig. 6(b) are reported. In panel A, we show the cold cavity situation: the sharp peak of R_1^s family is at a longer wavelength than the broad, almost critically coupled, R_2^s resonance. When

the pump laser starts sweeping across the R_2^p resonance, the intra-cavity pump intensity increases progressively, which in turn affects the probe doublet. Due to this the probe mode, R_2^s initially detunes faster than R_1^s, so that their relative detuning decreases (panel B).

Near the R_1^p switching point (panel C), the interference between the two resonances becomes critical, and the resonant feature R_1^s disappears completely. The detuning in the Fano interaction thus may be exploited as a mean to suppress one of the modes, permitting single mode operation in the range [12].

When the pump surpasses 1542 nm, de-locking from R_2^p, the power balance between the two pumped modes changes rapidly. As a consequence, now the R_1^p mode starts to heat more, pushing the R_1^s farther away in the red side (panel D). Finally, when the second resonance also is de-locked, both pump and probe spectra switch back to the initial unloaded condition (panel E). The whole experiment was repeated at different pump powers and on different couples of modes with analogous results.

C. Complete Mode Crossing

In Fig. 7, a complete crossing of a resonance doublet is reported, showing the behavior for different input powers. Note that the pump peaks of Figs. 6 and 7 are the same, while a different couple of probe peaks are analyzed. In the latter case, the cold cavity spectrum has the R_1^s peak on the blue side with respect to the wider R_2^s resonance ($\delta\omega_0^{12} = \omega_0^1 - \omega_0^2 > 0$). The figure reports the same experiment for different input powers.

At an input power of 0.5 W, the two resonances of the probe doublet start redshifting, and a progressive decrease in the relative detuning can be appreciated [Fig. 7(a)]. However, this input power is not enough to drive the probe spectrum into the $\delta\omega_0^{12} \leq 0$ condition. This happens because the pumped

doublet de-locks from the laser, and the spectrum jumps back to the cold cavity situation.

When the experiment is repeated for a 1.0 W of pump power [Fig. 7(b)], this time the pumped modes are dragged farther in the wavelength (late de-locking). This allows us to reach the $\delta\omega_0^{12} = 0$ situation for the probe doublet, which manifests as an electromagnetically induced transparency (EIT)-like probe spectrum.

Finally, we observed the complete mode crossing under a 2 W pump power [Fig. 7(c)]. In this case, the relative detuning of probe modes not only vanishes but also changes the sign ($\delta\omega_0^{12} < 0$). In Fig. 7(d) we plot selected spectra from Fig. 7(c) corresponding to three different cases of detuning $\delta\omega_0^{12}$: (A) the asymmetric Fano interference spectrum corresponds to the situation when the R_1^s resonance is on the blue side of R_2^s ($\delta\omega_0^{12} > 0$); (B) the zero-detuning situation results into an EIT-like symmetric spectrum, when the aligned R_1^s and R_2^s modes interfere destructively; (C) R_1^s finally surpasses R_2^s, giving rise to a Fano interference with sign-inverted relative detuning, $\delta\omega_0^{12} < 0$.

4. SIMULATIONS

In this section we describe the numerical simulations, which we have performed in order to validate the observed experimental results. Making use of a numerical solver, the solutions of Eqs. (15) and (16) are investigated. At first, the Δ_{ij} and Γ_{ij} matrices are estimated together with the parameters γ_j^{nr} and ω_j^o by fitting the cold cavity spectra of pumped doublet of resonances (the rightmost couple in Fig. 5). The g_{ij}^p matrix is then estimated up to an overall factor according to Section 2.A, making use of the FEM simulations shown in Fig. 2. The Δ_{ij} and Γ_{ij} matrices have been obtained using the same procedure as in Ref. [18]. The Δ_{ij} and Γ_{ij} matrices are calculated as $\bar{\Delta}\eta_{ij}$ and $\bar{\Gamma}\eta_{ij}$, respectively, where $\eta_{ij} = \eta_i\eta_j$ is the coupling weight matrix, and $\eta_{1,2}$ are the relative coupling weights coefficients with the waveguide such that $\eta_1^2 + \eta_2^2 = 1$. The values of η_i, $\bar{\Delta}$, and $\bar{\Gamma}$ for the pump resonances of Fig. 8 are reported in Table 1.

In a next step, the nonlinear pump equation, Eq. (15), is solved numerically to find the intensity distribution that generates the heat, in steady-state conditions, assuming the pump cold cavity spectrum parameters reported in Table 1 are constant during the evolution. The solution is obtained moving the laser from short to long wavelengths.

Figure 8(a) shows that good agreement was achieved between the experimental (black lines) and simulated (red dashed line) transmission of the pump. In Fig. 8(b) we show the experimental evolution of the probe spectrum as a function of the pump wavelength of panel (a). The experimental map is the same as in Fig. 7(b) and is reported here in order to facilitate the comparison with the simulated map.

The dynamic evolution of the relative coupling between the waveguide and the two radial family modes, which changes due to the thermo-optically altered refractive index $\delta n(r)$, is plotted in Fig. 8(c). We note that Eqs. (15) and (16) do not consider explicitly nonlinear variations of η_1, η_2, albeit the coupling among the waveguide, and the resonator is affected by thermal
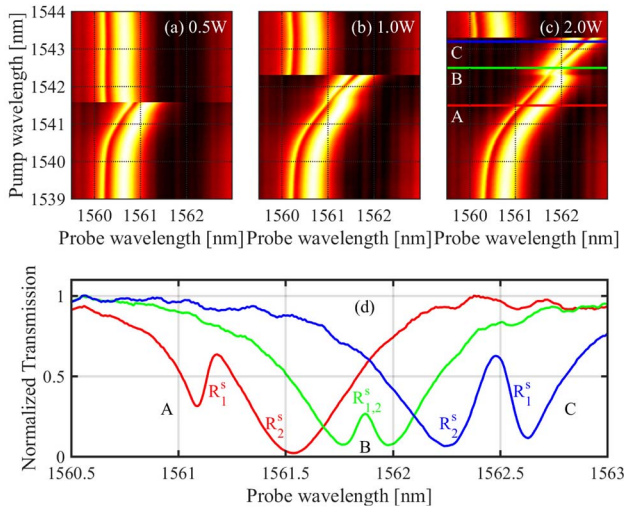
Fig. 7. Pump and probe experiments demonstrating a complete crossing of the modes. Panels (a), (b), and (c) represent the same experiment under different input power conditions of 0.5, 1, and 2 W, respectively. (d) The selected spectra, under 2 W pump, demonstrate three cases of the relative detuning, which changes from positive (A) to negative (C) passing through the $\delta\omega_0^{12} = 0$ condition (B). The probe spectrum time evolution, together with the pump dynamic transmission with input power 2.0 W is represented in Visualization 2.
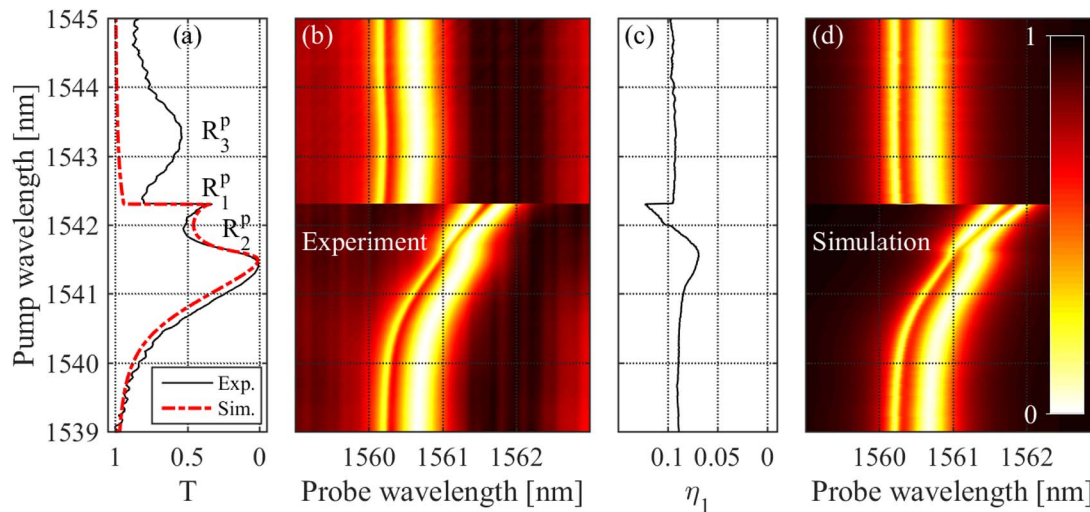
Fig. 8. Experimental and simulated data of the pump and probe experiment. (a) Experimental pump transmission spectrum of the loaded cavity (black line) is simulated (dashed red) by inserting the cold cavity fit parameters into Eq. (15). (b) Experimental transmission map as a function of both pump and probe wavelength is shown. (c) Relative coupling η_1 among the two radial family modes to the waveguide, extracted from results in panel (b). Successively, η_1 is used to compute the Γ and Δ matrices of Eq. (10) to also take into account the changes in the coupling induced by the thermally induced $\delta n(r)$. Panel (d) shows the transmission map as a function of both pump and probe wavelength using the simulated in (a) pump excitation for Eq. (16).

Table 1. Fit Parameters of the Cold Cavity Spectra of Both Pump and Probe Resonances, Used in the Simulations[a]

		R_1^p	R_2^p	R_1^s	R_2^s
η_i		0.0723	0.9974	0.0976*	0.9952*
γ_j^{nr}	[GHz]	4.400	20.581	5.558	28.01
ω_j^o	[THz]	194.532	194.374	192.15	191.92
g_{ii}/g_{11}		1.00	0.92	1.00	0.92
Δ	[GHz]	186.33		193.44	
$\bar{\Gamma}$	[GHz]	24.749		18.567	
g_{12}/g_{11}		0.90		0.90	
g_{11}	[GHz]	−150		−150	

[a]In the probe case, the reported starred (*) values of η_i are the initial cold cavity values, but their evolution under the effect of the thermal field, reported in Fig. 8(c), was used in the simulation.

detuning. The evolution of the relative coupling η_1^s is therefore obtained by fitting the experimental probe spectra. The probe equation, Eq. (16), is linear with respect to the parametric functions of pump intensities. Therefore, Eq. (16) is linearly solved for each pump wavelength, producing the 2D map reported in Fig. 8(d). The good accordance between the measured and calculated maps indicates that the developed theoretical model is capturing all the details of the physical phenomenon.

As a further comment, the relative detuning of the two probe resonances is driven by the ratio of the g_{11} and the g_{12} terms, which is 0.90 in our case, as shown by the values reported in Table 1. While this contrast could seem small for practical applications, it is worth noting that, in the reported experiments, both R_1^p and R_2^p families have been strongly excited, therefore enabling also the g_{22} term, which contrasts the detuning. A more pronounced detuning effect is expected when only one of the resonances is pumped, as is the case of

Fig. 6(b) in the region between Sections C and D, where, after the slow de-locking of R_2^p, the effect of R_1^p dominates, producing a clear shift. Furthermore, other geometries and materials could be considered. For example, in integrated wedge resonators, where the confinement factor varies sensibly between different radial mode families, a top cladding with a thermo-optic coefficient opposite to that of the guiding core can be exploited in order to increase the relative detuning of modes.

5. CONCLUSIONS

In this work, we have reported a joint theoretical and experimental study on the possibility to tune cavity resonances via optically driven material nonlinearities. We actuated the thermo-optical effect locally around the mode extension by means of strong optical pump field, while the cavity dynamics were monitored via weak probe signal. The effect of the thermal nonlinearity on the position and shape of the resonances has been exploited to tune the asymmetry of Fano resonances, realizing a complete mode crossing within a single doublet of modes. Moreover, we demonstrated the possibility to suppress one of these modes by fine tuning the system into a critical interaction condition.

Theoretically the resonator-waveguide system has been modeled via a set of nonlinear equations that take into account the local heating. The developed model was validated by numerical simulations, which are in excellent agreement with experimental results. Further improvements to the model are expected, taking into account the coupling variations induced by the thermo-optic effect also in the pump equations and possible nonlinear losses.

Our theoretical approach can be generalized and extended to other material nonlinearities and photonic systems. For example, it may be possible to exploit ultrafast Kerr nonlinearities

in order to achieve high-speed modulation of the spectral response in multimode resonator devices.

REFERENCES

1. K. J. Vahala, "Optical microcavities," Nature **424**, 839–846 (2003).
2. A. B. Matsko, *Practical Applications of Microresonators in Optics and Photonics* (CRC Press, 2009).
3. N. Sherwood-Droz and M. Lipson, "Scalable 3D dense integration of photonics on bulk silicon," Opt. Express **19**, 17758–17765 (2011).
4. M. Asghari and A. V. Krishnamoorthy, "Silicon photonics: energy-efficient communication," Nat. Photonics **5**, 268–270 (2011).
5. W. Bogaerts, P. De Heyn, T. Van Vaerenbergh, K. De Vos, S. Kumar Selvaraja, T. Claes, P. Dumon, P. Bienstman, D. Van Thourhout, and R. Baets, "Silicon microring resonators," Laser Photon. Rev. **6**, 47–73 (2012).
6. L. Maleki, A. B. Matsko, A. A. Savchenkov, and V. S. Ilchenko, "Tunable delay line with interacting whispering-gallery-mode resonators," Opt. Lett. **29**, 626–628 (2004).
7. L. Liu, R. Kumar, K. Huybrechts, T. Spuesens, G. Roelkens, E.-J. Geluk, T. de Vries, P. Regreny, D. Van Thourhout, R. Baets, and G. Morthier, "An ultra-small, low-power, all-optical flip-flop memory on a silicon chip," Nat. Photonics **4**, 182–187 (2010).
8. Q. Xu, B. Schmidt, S. Pradhan, and M. Lipson, "Micrometre-scale silicon electro-optic modulator," Nature **435**, 325–327 (2005).
9. M. A. Foster, J. S. Levy, O. Kuzucu, K. Saha, M. Lipson, and A. L. Gaeta, "Silicon-based monolithic optical frequency comb source," Opt. Express **19**, 14233–14239 (2011).
10. P. Dong, W. Qian, H. Liang, R. Shafiiha, N.-N. Feng, D. Feng, X. Zheng, A. V. Krishnamoorthy, and M. Asghari, "Low power and compact reconfigurable multiplexing devices based on silicon micro-ring resonators," Opt. Express **18**, 9852–9858 (2010).
11. Y. H. Wen, O. Kuzucu, T. Hou, M. Lipson, and A. L. Gaeta, "All-optical switching of a single resonance in silicon ring resonators," Opt. Lett. **36**, 1413–1415 (2011).
12. Y. H. Wen, O. Kuzucu, M. Fridman, A. L. Gaeta, L.-W. Luo, and M. Lipson, "All-optical control of an individual resonance in a silicon microresonator," Phys. Rev. Lett. **108**, 223907 (2012).
13. A. E. Miroshnichenko, S. Flach, and Y. S. Kivshar, "Fano resonances in nanoscale structures," Rev. Mod. Phys. **82**, 2257–2298 (2010).
14. Q. Xu, S. Sandhu, M. L. Povinelli, J. Shakya, S. Fan, and M. Lipson, "Experimental realization of an on-chip all-optical analogue to electromagnetically induced transparency," Phys. Rev. Lett. **96**, 123901 (2006).
15. C. Dong, C. Zou, Y. Xiao, J. Cui, Z. Han, and G. Guo, "Modified transmission spectrum induced by two-mode interference in a single silica microsphere," J. Phys. B **42**, 215401 (2009).
16. B. Li, Y. Xiao, C. Zou, Y. Liu, X. Jiang, Y. Chen, Y. Li, and Q. Gong, "Experimental observation of Fano resonance in a single whispering-gallery microresonator," Appl. Phys. Lett. **98**, 021116 (2011).
17. Q. Huang, Z. Shu, G. Song, J. Chen, J. Xia, and J. Yu, "Electromagnetically induced transparency-like effect in a two-bus waveguides coupled microdisk resonator," Opt. Express **22**, 3219–3227 (2014).
18. M. Ghulinyan, F. R. Manzano, N. Prtljaga, M. Bernard, L. Pavesi, G. Pucker, and I. Carusotto, "Intermode reactive coupling induced by waveguide-resonator interaction," Phys. Rev. A **90**, 053811 (2014).
19. G. Griffel, "Vernier effect in asymmetrical ring resonator arrays," IEEE Photon. Technol. Lett. **12**, 1642–1644 (2000).
20. U. Fano, "Effects of configuration interaction on intensities and phase shifts," Phys. Rev. **124**, 1866–1878 (1961).
21. T. Baak, "Thermal coefficient of refractive index of optical glasses," J. Opt. Soc. Am. **59**, 851–857 (1969).
22. F. Ramiro-Manzano, N. Prtljaga, L. Pavesi, G. Pucker, and M. Ghulinyan, "Thermo-optical bistability with Si nanocrystals in a whispering gallery mode resonator," Opt. Lett. **38**, 3562–3565 (2013).
23. M. Ghulinyan, R. Guider, G. Pucker, and L. Pavesi, "Monolithic whispering-gallery mode resonators with vertically coupled integrated bus waveguides," IEEE Photon. Technol. Lett. **23**, 1166–1168 (2011).
24. M. Ghulinyan, F. Ramiro-Manzano, N. Prtljaga, R. Guider, I. Carusotto, A. Pitanti, G. Pucker, and L. Pavesi, "Oscillatory vertical coupling between a whispering-gallery resonator and a bus waveguide," Phys. Rev. Lett. **110**, 163901 (2013).